Renewable Energy 133 (2019) 1011–1023

Contents lists available at ScienceDirect

Renewable Energy

journal homepage: www.elsevier.com/locate/renene

Improving CFD wind farm simulations incorporating wind direction uncertainty

Enrico G.A. Antonini*, David A. Romero, Cristina H. Amon

University of Toronto, Toronto, Canada

ARTICLE INFO

Article history:
Received 4 January 2018
Received in revised form
18 October 2018
Accepted 20 October 2018
Available online 29 October 2018

Keywords:
Wind farm
Wake losses
CFD RANS
Turbulence modeling
Wind direction uncertainty
Wake meandering

ABSTRACT

Accurate quantification of wake losses is crucial in wind farm economics. Computational Fluid Dynamics (CFD) has been proven to be a reliable solution to simulate many complex flows, but several studies showed that its effectiveness in wind farms simulations has not always been consistent. In this work, we investigate the causes for that inconsistency and propose a modeling framework to overcome them. A CFD model was developed using the actuator disk technique to simulate the wind turbines and the surface boundary layer approximation to simulate the ambient conditions. The developed CFD model was implemented for three different wind farms with publicly available experimental measurements. The predictions of CFD model were post-processed with an innovative method that uses a Gaussian-weighted average of a set of CFD results for different wind directions to account for the wind direction uncertainty in the experimental data. Our results show that the proposed method significantly improves the agreement of the CFD predictions with the available experimental observations. These results suggest that the discrepancies between CFD predictions and experimental data reported in previous works, attributed to inaccuracy of the CFD models, can be explained instead by the uncertainty in the wind direction reported in the data sets.

1. Introduction

Wind farms are nowadays producing the majority of the worldwide wind energy. The installed global capacity at the end of 2016 was of about 490 GW [1] and this capacity is projected to double in the coming years. As wind energy experiences this tremendous growth, a complete understanding and characterization of wind farm phenomena have become one of the main goals among the wind energy community.

When wind turbines are arranged in large wind farms, there will inevitably be a loss of power output due to wind turbine wakes [2,3]. These wakes are the result of the energy extraction performed by the wind turbines. Within a wind farm, wind speeds do not recover to their freestream value after encountering the first turbine (or row of turbines) and this reduces the power production of the downstream turbines [4]. Although this is a well-known phenomenon, power losses due to wakes are difficult to predict accurately due to the temporal and spatial variability of the wind speed and direction [5]. Turbulence, atmospheric stability and terrain features also play a significant role in the wake development and, consequently, in the farm performance [6,7].

Accurate quantification of power losses due to wind turbine wakes in different wind climates and wind farm layouts is essential for optimal wind farm design. Different approaches exist to model wind turbine wakes, namely, analytical and numerical models [8]. Analytical wake models (also called kinematic wake models) use self-similar velocity deficit profiles obtained from experimental and theoretical work on co-flowing jets [9]. Despite the advantage of being simple and computationally efficient, their predictions cannot take into account all the complex fluid mechanics that occur in wind farms. Numerical models, instead, rely on Computational Fluid Dynamics (CFD) [5] and offer higher accuracy and flexibility to account for different ambient conditions and terrain features. Recent research has indeed focused on the use of CFD models for the optimal design of wind farms [10,11].

A significant part of CFD models uses large eddy simulations

* Corresponding author.
E-mail address: enrico.antonini@mail.utoronto.ca (E.G.A. Antonini).

https://doi.org/10.1016/j.renene.2018.10.084
0960-1481/

(LES) to solve the flow field [5]. Although LES models have a high level of fidelity when simulating turbulent flows, their use is still limited by the extensive computational resources they require to solve the flow equations. The vast majority of CFD models are instead based on Reynolds-averaged Navier-Stokes (RANS) equations to solve the flow field. The use of this time-averaging procedure reduces the computational cost of the simulations, but creates the need for additional turbulence models to close the system of equations.

Different turbulence models have been used in wind turbine and wind farm simulations to predict wake velocities and power output. One of the most used turbulence models is the $k-\varepsilon$ model, which has been implemented in many wind turbine and farm studies [12–15]. Simulations using the $k-\varepsilon$ model showed good agreement with experimental wake measurements when the CFD codes used the parabolic RANS equations (i.e., the pressure gradient is neglected and the velocity profile is prescribed behind the wind turbine), whereas higher discrepancies were found when the elliptic RANS equations (i.e., full equations without any simplification) were employed. Réthoré [13] suggested that the cause of these discrepancies may lie in the limited validity of the eddy viscosity assumption (Boussinesq approximation) in the near wake region. Another turbulence model widely used in wind farm simulations is the $k-\omega$ model, which was extensively studied by Prospathopoulos et al. [16,17]. Similarly to the $k-\varepsilon$ model, the simulations using the $k-\omega$ model showed poor agreement with experimental observations. One of the most promising turbulence models, the *SST* $k-\omega$ model, widely used in aeronautical applications, was recently tested in two wind farm studies [18–20] where it showed better agreement with experimental data than the standard $k-\varepsilon$ and $k-\omega$ models. Lastly, a different approach that does not make use of the Boussinesq hypothesis and computes directly the Reynolds stresses is the Reynolds stress model (RSM), which was first tested by Cabézon et al. [14] for wake effect predictions and compared with the standard $k-\varepsilon$ model.

Although RANS turbulence modeling in the context of wind turbine wake predictions has been widely studied in literature, its effectiveness has not been always consistent. A general level of agreement exists in identifying the $k-\varepsilon$ and $k-\omega$ models as the least accurate for wake predictions. For this reason, many authors have proposed modifications of the original models to improve agreement with experimental data [14,17,18,21,22]. However, some studies showed that CFD wake models employing the original $k-\varepsilon$ and $k-\omega$ models were able to provide good agreement with experimental observations. For instance, in Refs. [3,23] the $k-\varepsilon$ model was used with the full RANS equations resulting in accurate predictions of the power production of turbines operating in wake conditions. In addition, the $k-\varepsilon$ and $k-\omega$ models were shown to be as accurate as the *SST* $k-\omega$ and Reynolds stress models in at least two studies focusing on far wake predictions [17,19,20].

The reason for this inconsistency of wake model predictions found in some studies is very likely related to unsteady and large-scale phenomena not taken into account in the simulations that, while affecting the experimental measurements, are not taken into account in the simulations [24]. RANS wake models are usually set up as steady simulations whereas experimental measurements are affected by unsteady phenomena that naturally occur in ambient conditions [25]. These unsteady phenomena can be quantified by the uncertainty that is associated with the statistics of wind speed and direction. Because wind speed variability is accounted for in RANS simulations by the turbulence models and, in particular, by the turbulence kinetic energy, the most significant contribution to the aforementioned limitations is therefore expected to be given by the wind direction variability. This variability has, in fact, been shown to have a strong impact on turbine-wake characteristics, such as velocity deficit [26]. Direct methods currently available to account for these unsteady flow phenomena are unsteady RANS simulations (URANS) or LES, which are computationally more expensive by orders of magnitude.

In the present work, we aim to investigate the limitations and inconsistency of the RANS wake models and to propose an innovative approach to overcome them. A CFD model was initially developed using the actuator disk technique to simulate the wind turbines and the surface boundary layer approximation to simulate the ambient conditions. The developed CFD model was implemented to simulate three different wind farms, namely, Sexbierum, Nibe, and Horns Rev, with publicly available experimental measurements. The main turbulence models present in literature and available in common CFD software packages, namely, the $k-\varepsilon$, $k-\omega$, *SST* $k-\omega$ and Reynolds stress models, were used to close the RANS equations and their results compared. Following the same approach of other studies (e.g., [12–14,16–18]), the validation of the developed CFD model with different turbulence closures was conducted by comparing the CFD predictions with both observed wind speeds and power production of the selected wind farms.

To account for the wind direction variability, we subsequently introduced a method to model the wind direction uncertainty using simulation ensembles, i.e., a set of CFD results for different wind directions is post-processed to generate a single CFD prediction. Our results showed that RANS simulations using the *SST* $k-\omega$ and Reynolds stress models were consistently more accurate when considering wind speeds and power production in the wake region of the considered wind farms. These are therefore to be preferred over the $k-\varepsilon$ and $k-\omega$ models. The result also showed that the proposed approach for considering wind direction uncertainty was able to overcome the limitations and inconsistency of previous works. Overall, this method improved the agreement between the experimental data and CFD model with the suggested turbulence closures by accounting for the uncertainty in the wind direction reported in the data sets.

The outline of the paper is the following. In Section 2, we present the case studies that will be used to test and validate the CFD model and the innovative post-processing technique. The CFD methodology is described in Section 3 along with an overview of turbulence models used to close the RANS equations. Section 4 describes the modeling assumptions for the wind turbines and the surface boundary layer that are integrated in the CFD model. In Section 5, we provide details about the numerical implementation and boundary conditions of the CFD model. The innovative post-post-processing technique, called in this paper MUSE (Modeling Uncertainty with Simulation Ensembles), is presented in Section 6. Section 7 compares the results obtained directly from the RANS simulations and the results obtained after the averaging process with the MUSE method. Conclusions are summarized in Section 8.

2. Case studies

The validation of the proposed approach for CFD models, which will be described in the following sections, was conducted using

Table 1
Wind turbine characteristics and wind conditions of Sexbierum and Nibe wind farms.

Wind farm	D [m]	H [m]	U_{inf} [m/s]	TI_x [%]	C_T [–]
Sexbierum	30.1	35	10	10	0.75
Nibe	40	45	8.5	10	0.82
Horns Rev	80	70	8	8	0.80

the experimental data sets from the Sexbierum [27], Nibe [28], and Horns Rev [6] wind farms. Table 1 summarizes the wind turbine characteristics and wind conditions.

2.1. Sexbierum wind farm

The Dutch Experimental Wind Farm at Sexbierum is located in the Northern part of The Netherlands at approximately 4 km distance from the seashore. The wind farm is located in flat homogeneous terrain, mainly grassland used by farmers. The wind farm has a total of 5.4 MW installed capacity consisting of 18 turbines of 300 kW rated power each. The wind turbines in the wind farm are HOLEC machines with three WPS 30/3 blades, a rotor diameter of 30.1 m, and a hub height of 35 m. Performance curves are reported in Fig. 1a. The campaign concerned measurement of the wind speed, turbulence and shear stress behind a single wind turbine at distances of 2.5, 5.5 and 8 rotor diameters, respectively. The free stream wind conditions at hub height were $U_{inf} = 10$ m/s and $TI_x = 10\%$. For these conditions, the thrust coefficient was $C_T = 0.75$. The wind direction bin width was 2.5°.

2.2. Nibe wind farm

The Nibe wind farm is located on a coastal site near Aalborg in the norther Jutland, Denmark. It is constituted by two machines (A and B) located 200 m apart from each other along an approximately North-South axis, which runs parallel to the coast line. To the west there is a fetch of at least 6 km over open, shallow water. On the landward site, the ground surrounding the site is flat, grass-covered, and free of significant obstacles. The two wind turbines are almost identical, both with a rated power of 630 kW. The rotor diameter is 40 m, the hub height is 45 m. Performance curves are reported in Fig. 1b. The data examined here correspond to the turbine B operating alone, and measurements of wind speed and turbulence are available behind the turbine at distances of 2.5, 4 and 7.5 rotor diameters, respectively. The free stream wind conditions at hub height were $U_{inf} = 8.5$ m/s and $TI_x = 10\%$. For these conditions, the thrust coefficient was estimated to be $C_T = 0.82$. The wind direction bin width was 2.5°.

2.3. Horns Rev wind farm

The Horns Rev wind farm is located 14 km from the west coast of Denmark. It has a rated capacity of 160 MW comprising 80 wind turbines, which are arranged in a regular array of 8 by 10 turbines. The wind turbines are installed with an internal spacing along the main directions (West-East) of 7*D*, whereas the diagonal wind turbine spacing is either 9.4*D* or 10.4*D*. The wind farm comprises Vestas V80 turbines, which are 2 MW pitch-controlled, variable speed wind turbines with an 80 m diameter and a 70 m hub height.

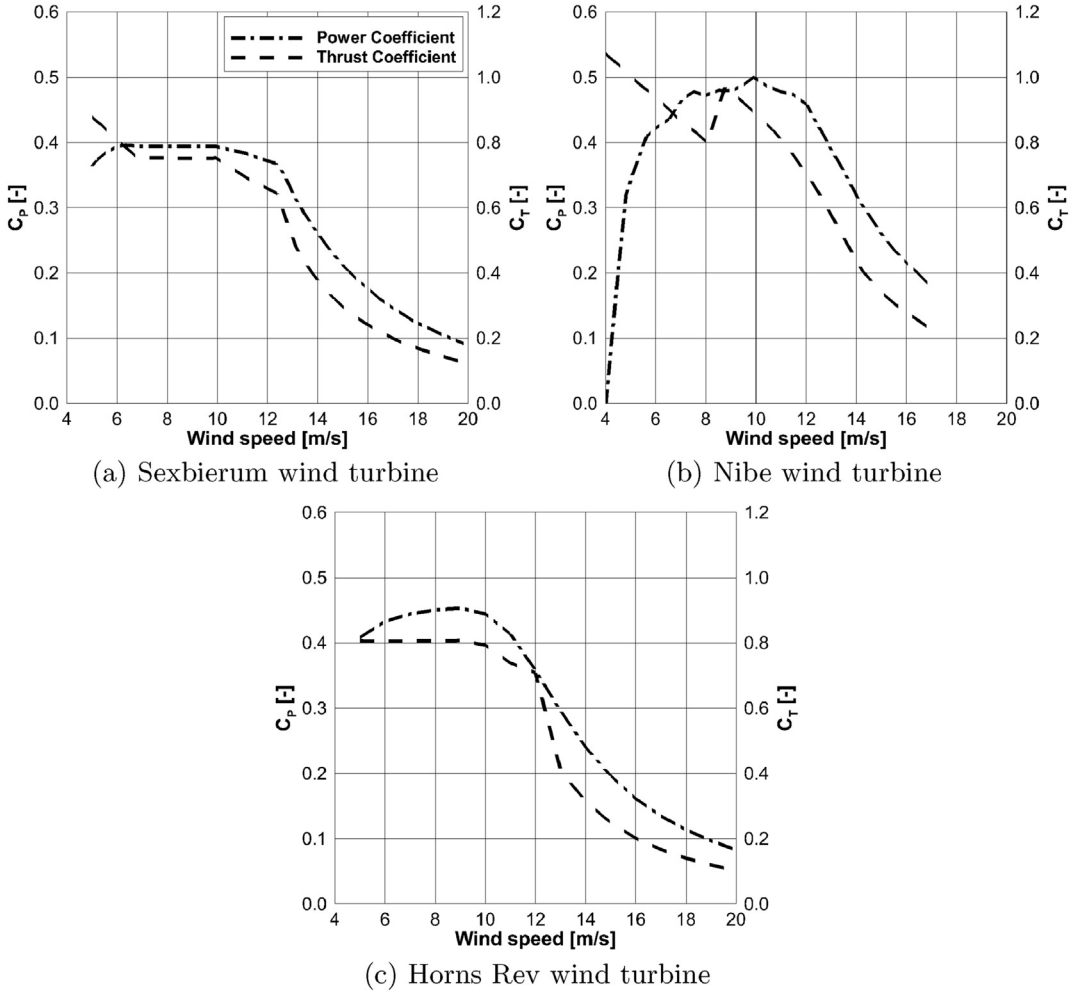

Fig. 1. Performance curves of the Sexbierum, Nibe, and Horns Rev wind turbines.

The performance of these turbines is reported in Fig. 1c. The data from the measurement campaign include the power output from the different rows of wind turbines and for different wind directions and sectors. In this work, two turbines were considered, namely, the turbines 07 and 17, which are 7D apart along the West-East direction with the turbine 07 facing undisturbed winds coming from West. The power measurements as a function of wind direction are taken from Ref. [29] where the free stream wind conditions were $U_{inf} = 8$ m/s and $TI_x = 8\%$. For these conditions, the thrust coefficient was estimated to be $C_T = 0.80$. The wind direction bin width was 5°.

3. CFD modeling

Reynolds-averaged Navier-Stokes (RANS) equations for incompressible, steady flows are chosen as the basis of the simulation model in this study. They require additional turbulence modeling to solve the nonlinear Reynolds stress term and to close the system of equations. The set of equations is composed of the continuity equation,

$$\frac{\partial U_i}{\partial x_i} = 0, \tag{1}$$

and three momentum equations,

$$U_j \frac{\partial U_i}{\partial x_j} = -\frac{1}{\rho}\frac{\partial p}{\partial x_i} + \frac{\partial}{\partial x_j}\left[\nu\left(\frac{\partial U_i}{\partial x_j} + \frac{\partial U_j}{\partial x_i}\right) - \overline{u_i u_j}\right] + \frac{f}{\rho}, \tag{2}$$

where $U_{i,j}$ is the mean velocity component, p is the mean pressure, ρ and ν are the fluid density and kinematic viscosity, respectively, f is the source term, and i, j are indexes over the coordinate directions. Transport equations for turbulence quantities are employed to compute the Reynolds stress terms, $\overline{u_i u_j}$, and their number depends on the particular choice of the turbulence model. OpenFOAM [30] is employed to solve this set of equations, using a control-volume-based technique to transform the governing flow equations into algebraic expressions that can be solved numerically. The discretization of the governing equations is based on the second-order upwind scheme, which is applied for the interpolation of velocities and turbulent quantities. The semi-implicit method for pressure-linked equations (SIMPLE) algorithms is used to solve simultaneously the set of equations by an iterative scheme.

3.1. Turbulence modeling

Four different turbulence models are used to close the RANS equations and compared to each other: $k-\varepsilon$, $k-\omega$, SST $k-\omega$, and Reynolds stress models. A more detailed description of the constitutive equations of the turbulence models used in this study can be found in Ref. [20].

The standard $k-\varepsilon$ turbulence model, first developed by Jones and Launder [31] and subsequently revised by Launder and Sharma [32], is currently the most widely used model in many fields [33]. The model is based on the turbulent-viscosity hypothesis (Boussinesq approximation) that relates the Reynolds stresses to the mean flow via the eddy viscosity. In spite of its broad rage of applicability and accurate results for simple flows, the $k-\varepsilon$ model has shown some limitations: it can be quite inaccurate for complex flows, in particular in the presence of large adverse pressure gradients [34]. Also, special near-wall treatments are usually required since the model has been shown to underperform in near-wall regions.

In this study, we adopt the standard $k-\omega$ model formulated by Wilcox [35] which, similarly to the $k-\varepsilon$ model, relies on the Boussinesq approximation to calculate the Reynold stresses. The $k-\omega$ model has been shown to perform better than the $k-\varepsilon$ model for boundary-layer flows, both in its treatment of the viscous near-wall region and in its accounting for the effects of streamwise pressure gradient [33]. However, the model showed problems when dealing with non-turbulent free-stream boundaries so that special boundary conditions are usually required. Also, it was shown that the $k-\omega$ model overpredicts the level of shear stress in adverse pressure-gradient boundary layers [34].

The shear-stress transport (SST) $k-\omega$ turbulence model was formulated by Menter [36] and has been found to be quite effective in predicting many aeronautical flows [37]. The reason for this is that it was designed to yield the best behavior of the $k-\varepsilon$ and the $k-\omega$ models: it retains the robust and accurate formulation of the Wilcox $k-\omega$ model in the near wall region, and takes advantage of the freestream independence of the $k-\varepsilon$ model in the outer part of the boundary layer. A blending function takes care of the switch between the two models according to the distance from a wall. A new definition for the turbulence viscosity was introduced by Menter to prevent the tendency to overestimate the shear stress intensity in adverse pressure-gradient boundary layers.

In the Reynolds stress models, the individual Reynolds stresses are directly computed and consequently the turbulent-viscosity hypothesis is not needed. Different formulations have been used to model the terms in the transport equations of the Reynolds stresses [38,39]. However, in this work the Gibson-Launder (GB) model [40] was chosen because it was developed and calibrated specifically to simulate atmospheric boundary layers. The RSM has six equations to compute each of the six Reynolds stresses and an equation for the turbulent dissipation rate. Thanks to the calculation of all six Reynolds stresses, the model can accurately predict anisotropic turbulent flows, which is an important advantage compared to the eddy viscosity models limited by the Boussinesq approximation and the assumption of isotropic turbulence. On the other hand, the RSM requires significantly more computational time compared to the simpler two-equation models.

3.1.1. Application-specific turbulence model constants

The commonly used values for the coefficients of the turbulence models previously described have been calibrated on several and various experimental data sets, and therefore represent a compromise to give the best performance for a wide range of flow conditions [33]. The conditions that a wind turbine simulation has to deal with represent a particular subset of the entire range of the turbulence model applicability. In particular, two main phenomena occurring in this application can be identified: the surface boundary layer (SBL) and the wake generated by the wind turbine that propagates in a SBL. Taking this into account, it is possible to reduce the range of applicability of the turbulence models to the particular flow characteristics of wind farms in the surface boundary layer by recalibrating the turbulence model constants based on experimental measurements. For example, Antonini et al. [19,20] derived and tested consistent turbulence model constants for each of the aforementioned turbulence models for SBL and wind turbine simulations (see Table 2). In this work, we used these constants for all our predictions, so that our results reflect the most-accurate versions of each turbulence model, recalibrated for our specific application.

4. Wind turbine and surface boundary layer modeling

This section provides a description of the approach used to model in our computational domain the wind turbines and the surface boundary layer where the turbines operate.

Table 2
Turbulence model constants for SBL and wind turbine simulations [19,20].

Turbulence model	Turbulence constants		
$k-\varepsilon$	$C_\mu = 0.0333$	$C_{1\varepsilon} = 1.42$	$C_{2\varepsilon} = 1.83$
		$\sigma_k = 2.25$	$\sigma_\varepsilon = 2.25$
$k-\omega$	$\beta^* = 0.0333$	$\alpha = 0.42$	$\beta = 0.0277$
		$\sigma^* = 0.45$	$\sigma = 0.45$
SST $k-\omega$	$\beta^* = 0.0333$	$\gamma_1 = 0.42$	$\beta_1 = 0.0277$
		$\sigma_{k1} = 0.45$	$\sigma_{\omega 1} = 0.45$
		$\gamma_2 = 0.42$	$\beta_2 = 0.0277$
		$\sigma_{k2} = 0.45$	$\sigma_{\omega 2} = 0.45$
RSM	$C_\mu = 0.0333$	$C_{1\varepsilon} = 1.42$	$C_{2\varepsilon} = 1.83$
		$\sigma_R = 0.8197$	$\sigma_\varepsilon = 2.25$
		$C_1 = 1.8$	$C_2 = 0.6$
		$C'_1 = 0.5$	$C'_2 = 0.3$

4.1. Wind turbine modeling

The wind turbine was modeled as an actuator disk which is characterized by a cylindrical volume, defined by the rotor swept area, where a distributed force, defined as axial momentum source, *F*, is applied. The main limitation of this model is that it does not provide a detailed description of the wind turbine geometry and therefore cannot capture the flow dynamics occurring on the rotor blades. However, it is able to capture adequately the wake effect generated by the wind turbine and to compute its power output, as required for the employment in wind turbine and wind farm simulations [13,41,42]. From the definition of thrust coefficient, it can be derived that the axial force is a function of the reference wind speed:

$$F = \frac{1}{2}\rho\frac{\pi D^2}{4}C_T U_{ref}^2, \tag{3}$$

where ρ is the air density, D is the rotor diameter, U_{ref} is the upstream wind speed, and C_T is the thrust coefficient, obtained from the thrust coefficient curve of the wind turbine at the specified U_{ref}. The power generated can be computed as the product of the axial force and the average velocity over the actuator disk volume V:

$$P = F\overline{U_x} = F\frac{1}{V}\int_V U_x dV. \tag{4}$$

In the case of wind turbines that operate in the wake of others, the value for the upstream wind speed is not readily available. Ideally, the reference wind speed for a turbine operating in wake condition is the speed that would be present at the turbine location without the turbine itself. Evaluating this speed would require therefore an additional simulation for each given wind boundary condition. Because of the high computational cost associated, two different approaches were used in literature to estimate the reference wind speed with simpler procedures. A common choice is to use the wind speed upstream of the rotor, at a distance of one ($1D$) or two ($2D$) rotor diameters as an estimate of the reference speed. However, this method cannot always guarantee an accurate estimation, so a validation step is typically recommended on a case-by-case basis. A different approach was introduced by Prospathopoulos et al. [17], which is based on an iterative calculation that uses the definition of the axial induction factor, a, and thrust coefficient curve of the specific wind turbine. In the present work, however, the authors chose to calculate the reference wind speed using the ideal method: an additional simulation for each given wind boundary condition was run to calculate the speed that would be present at the turbine location without the turbine itself. This procedure was conducted only for the case of multiple wind turbines, and it allowed to have the most accurate solution for the reference wind speed.

4.2. Surface boundary layer modeling

The atmospheric boundary layers (ABL) is used to model the wind conditions and characteristics usually encountered in real wind turbine and wind farm flows. For a homogeneous and stationary flow, the wind shear profile can be described, according to Panofsky and Dutton [43], as:

$$\frac{\partial U_x}{\partial z} = \frac{u_*}{\kappa l}, \tag{5}$$

where U_x is the mean streamwise wind speed, z is the height above ground, u_* is the local friction velocity, l is the local length scale, and κ is the von Kármán constant (≈ 0.4). Within the ABL, the friction velocity decreases with z, vanishing at the edge of the ABL according the following relation:

$$u_* = u_{*0}\left(1 - \frac{z}{z_{max}}\right)^\alpha, \tag{6}$$

where z_{max} is the height of the ABL and α depends on the state of the boundary layer, ranging from 2/3 to 3/2 [44]. The height of an ABL can extend up to some kilometers, depending on the atmospheric stability [43]. The first 10% of the ABL, which is usually called the surface boundary layer (SBL), can be approximated by a constant friction velocity equal to u_{*0}. Also, in the SBL, the length scale is assumed equal to the height ($l_{SL} = z$).

The length scale, l, is influenced by the atmospheric stability, which describes the combined effects of mechanical turbulence and heat convection, and the height of the ABL [43]. Three classes of atmospheric stability can be defined: unstable, neutral, and stable conditions. The experimental data set for two of the case studies analyzed in this work, Sexbierum and Nibe, was reported to experience neutral or near-neutral conditions, whereas, for the Horns Rev case, the experimental measurements were recorded under unstable conditions. In spite of the substantial difference in the phenomena that drive the different stability conditions, the measurements obtained under neutral and unstable conditions are usually very close to each other in terms of both wind speed/power production and turbulence intensity. This can be seen with the measurement campaign conducted at the Horns Rev wind farm [6], where neutral and unstable conditions are even grouped together because of their similarity. For this reason, the case studies analyzed in this work will take into account only the surface boundary layer under neutral conditions, which is a reasonable approximation for the lowest part of the atmospheric boundary layer where wind turbines operate [43].

Under the previously discussed hypothesis, a logarithmic velocity profile can be derived from Eq. (5) by integration:

$$U_x = \frac{u_{*0}}{\kappa} ln\left(\frac{z}{z_0}\right), \tag{7}$$

where z_0 is the surface roughness length. This parameter is solely used for describing the wind speed profile, in fact, it is not a physical length, but rather a length scale representing the roughness of the ground (reference values for different terrain types can be found in Ref. [43]). The friction velocity can be calculated once a reference velocity is known at a specific height:

$$u_{*0} = \frac{\kappa U_{x,ref}}{ln\left(\frac{z_{ref}}{z_0}\right)}. \tag{8}$$

Introducing the equation for the wind profile into the turbulence models, it can be derived that the turbulent kinetic energy,

turbulent dissipation rate, and specific dissipation rate have the following expressions, respectively [16,45]:

$$k = \frac{u_{*0}^2}{\sqrt{C_\mu}}, \quad \varepsilon = \frac{u_{*0}^3}{\kappa z}, \quad \omega = \frac{u_{*0}}{\sqrt{\beta^* \kappa z}}. \tag{9}$$

Panofsky and Dutton [43] extrapolated average values for the Reynolds stresses from different experimental data sets and these are given as a function of the friction velocity: $\overline{u_x u_x} = (2.39 u_{*0})^2$, $\overline{u_y u_y} = (1.92 u_{*0})^2$, $\overline{u_z u_z} = (1.25 u_{*0})^2$, $\overline{u_x u_z} = -u_{*0}^2$, $\overline{u_x u_y} = \overline{u_y u_z} = 0$. From the value of the xx-Reynolds stress, Prospathopoulos et al. [16] derived a useful relation between the surface roughness length and the streamwise turbulence intensity, TI_x, which is a common parameter used to characterize the flow turbulent conditions. Following the definition of turbulence intensity, it is possible to write:

$$TI_x = \frac{\overline{u_x}}{U_{x,ref}} = 2.39 \frac{u_{*0}}{U_{x,ref}}. \tag{10}$$

Introducing Eq. (8) on the right hand side of Eq. (10), it is possible to rearrange the equation in order to find the value of the surface roughness length as a function of the turbulence intensity:

$$z_0 = z_{ref} exp\left(\frac{-0.980}{TI_x}\right). \tag{11}$$

Starting from the definition of turbulent kinetic energy, it is also straightforward to derive a relation between the turbulent kinetic energy and the streamwise turbulence intensity:

$$k = \frac{1}{2}\left(\overline{u_x u_x} + \overline{u_y u_y} + \overline{u_z u_z}\right) = 5.48 u_{*0}^2 = 0.959 TI_x^2 U_{x,ref}^2. \tag{12}$$

5. Numerical setup

The computational domain and mesh of the three cases were generated with *blockMesh* and *snappyHexMesh*, two mesh utilities of OpenFOAM for mesh generation and refinement, respectively. The Cartesian coordinate system is defined with x, y, and z being respectively the streamwise, lateral and vertical directions. Fig. 2 illustrates schematic layouts of the domain used for the Sexbierum and Nibe cases. The dimensions of the domain are a function of the rotor diameter (D). The domain includes the actuator disk region and a refined region surrounding the disk with a double mesh resolution in order to capture the most significant gradients in the flow field. For the Horns Rev case, two turbines were instead included in the domain.

The dimensions of the domain were carefully determined in order to not influence the flow-field solution and to avoid unnecessary domain regions. A detailed sensitivity analysis can be found in Refs. [19,20] and the same procedure was followed in this work. The upstream distance from the wind turbine and the domain height were set to 3D and 5D, respectively. For the Horns Rev case, the second wind turbine was place at a distance of 7D downstream. The other dimensions were basically chosen in order to have the flow-field solution as far as the experimental measurements are available for comparison. The global grid spacing was set to 0.1D, whereas the resolution in the refined region surrounding the wind turbine was as double as the global resolution in order to capture the main gradients in the flow field. In the region close to the wall, the resolution was also higher: the first cell at the wall was fixed to a height of 0.01D and this value was progressively increased

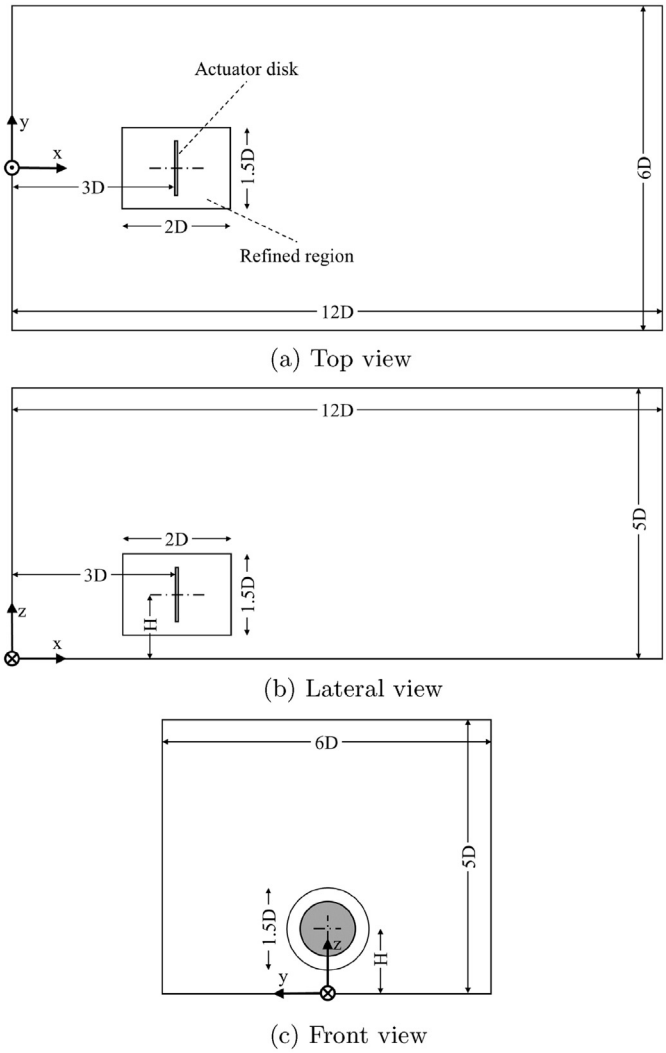

Fig. 2. Schematic layouts of the domain.

moving away from the wall, up to the size given by the global resolution. The height of the region where this mesh refinement took place was 0.5D. For the solution of the RANS equations, the convergence criterion was set so that the residuals of all the equations were below 10^{-5}.

5.1. Boundary conditions

The inlet boundary condition was defined with the equations relative to the SBL. Given the flow characteristics, i.e., U_{inf}, TI_x, and H, the values for z_0 and u_{*0} were derived with Eqs. (8) and (11). The velocity, turbulence kinetic energy (or Reynolds stresses), and turbulence dissipation rate (or specific dissipation rate) were then prescribed according to Eqs. (7) and (9), depending on the turbulence model used. The outlet boundary condition was defined as a pressure outlet, with zero gradient for the velocity and turbulence quantities. The top boundary condition was defined by prescribing constant values of velocity, turbulence kinetic energy (or Reynolds stresses), and turbulence dissipation rate (or specific dissipation rate) at the domain height, whereas zero gradient was set for the pressure. The side boundary condition was defined as zero gradient for all the variables. The ground was defined as a rough wall, with wall functions that took care of the turbulence quantities.

5.2. Wall functions

A proper treatment of the ground surface is essential to correctly simulate SBL flows. A general requirement of CFD simulations consists in having a very fine mesh in proximity of any surface in order to capture the large velocity gradients and to compute a correct wall shear stress. In SBL simulations, this is impossible because the surface roughness prevents a full solution of the boundary layers. In fact, the first wall-adjacent cell should be at least the double of the surface roughness, which is in conflict with the requirement of a high mesh resolution. In these cases, wall functions based on log-law boundary layers for rough walls are used to calculate the turbulent viscosity and wall shear stress. Blocken et al. [46] discussed the problem of the wall treatment for these particular flows, suggesting remedies when the simulations are run with ANSYS Fluent or CFX, which adopt wall functions based on an equivalent sand-grain roughness, k_S, equivalent to approximately $30z_0$. In contrast, OpenFOAM uses a wall function based on the actual surface roughness length, z_0, that is derived from Eq. (7). This was used in the present work and allowed us to have a higher resolution close to the wall than the one possible with ANSYS Fluent and CFX. A value of approximately $0.01D$ for the height of the first cell at the wall was found to guarantee a correct simulation of SBL flows, achieving horizontally homogeneity (i.e., zero streamwise gradients) of the SBL in an empty domain. This value is also consistent with other works present in literature [14,17].

6. Modeling uncertainty with simulation ensembles (MUSE)

The results from simulations run with steady conditions are not directly comparable with results from field measurements. The reason is that field measurements are given as an average of values in a certain period of time, classified by a specific range of wind direction, wind speed, turbulence intensity and atmospheric stability. Within each period, wind intensity and direction change in time and produce an uncertainty associated with the average value of a measuring period. The wind direction variability is expected to have the most significant impact on turbine-wake characteristics, such as velocity deficit [26]. Causes of wind direction uncertainty can be identified in spatial and temporal de-correlation of the wind direction between the measurement and the turbine locations, large-scale turbulence of the incoming boundary layer flow that drives the meandering of the wakes [47], and sensor inaccuracy and uncertainty, among others [6]. Gaumond et al. [48] suggested that the discrepancies of numerical simulations for narrow wind direction sectors found in different studies are not caused by wake modeling inaccuracies but rather by the large wind direction uncertainty included in the data sets. Subsequently, Gaumond et al. [24] proposed a method to take into account the wind direction uncertainty post-processing the results from analytical wake models, improving the agreement of the results. This technique is applied in this study in order to compare the results from the CFD wake model with field measurements. With this approach, we propose to Model Uncertainty with Simulation Ensembles (MUSE): we show that a weighted average of several CFD RANS results covering a wide range of wind directions can effectively take into account the large-scale flow phenomena causing wind direction variability. As such, this method can be considered a computationally faster alternative to URANS or LES models, which are usually needed to simulate large-scale flow phenomena with transient changes in the flow field.

The wind direction uncertainty is assumed to have a Gaussian distribution around an average value. The probability density of the Gaussian distribution relative to a wind direction, θ, is thus:

$$f_g(\theta) = \frac{1}{\sigma_\theta\sqrt{2\pi}}\exp\left[-\frac{\left(\theta-\overline{\theta}\right)^2}{2\sigma_\theta^2}\right], \tag{13}$$

where $\overline{\theta}$ is the average wind direction and σ_θ is the standard deviation associated with the wind direction. This standard deviation is generally available for a given site from the measurement campaign conducted for wind resource assessment and allows to consider local characteristics of wind direction variability. For instance, for the Nibe wind farm, the standard deviation was $\sigma_\theta = 5^\circ$. For the Sexbierum wind farm, the wind direction uncertainty was not reported in the data set. Nevertheless, Peña et al. [49] derived from numerical simulations of the same case and experimental measurements of a different site with similar wind conditions a value in the range of $2^\circ - 3.5^\circ$. A value of 3° is therefore adopted in this study. Lastly, for the Horns Rev wind farm, Hansen et al. [6] stated that the wind direction uncertainty associated with the measurements could reach values of more than 7° because of the large distance between the wind measuring station and the operating wind turbines. However, Gaumond et al. [24] in their post-processing calculations with the wind direction uncertainty found that values in the range of $5^\circ - 7^\circ$ provided better wake deficit predictions. Therefore, in this study, a value of 6° was chosen as a trade-off between the previous considerations.

Once the flow field is obtained from the simulations, the velocity downstream the wind turbine can be expressed as a function of the wind direction, θ, and the downstream distance, d, given the aforementioned input conditions:

$$U = f(\theta, d). \tag{14}$$

A method to model wind direction uncertainty with simulation ensembles is then used: a weighted average is applied to a set of CFD results for different wind directions to generate a single CFD prediction based on the given standard deviation associated with the data set. The resulting velocity for a specific direction, $\overline{\theta}$, and distance, d, is obtained as a weighted averaged of the simulated velocities in the range of $\overline{\theta}\pm 3\sigma_\theta$ at the same distance, where the weights are given by the Gaussian distribution:

$$U\left(\overline{\theta}, d\right) = \int_{\overline{\theta}-3\sigma_\theta}^{\overline{\theta}+3\sigma_\theta} U(\theta, d) f_g(\theta) d\theta. \tag{15}$$

The process is repeated for all the directions at the same downstream distance. In a similar way, this method can be applied to any quantity of interest that depends on the wind direction and for which time-averaged experimental measurements are available. As such, it can also be applied to the power generation of a turbine operating in wake conditions. The resulting power can be calculated as follows:

$$P\left(\overline{\theta}, d\right) = \int_{\overline{\theta}-3\sigma_\theta}^{\overline{\theta}+3\sigma_\theta} P(\theta, d) f_g(\theta) d\theta. \tag{16}$$

Fig. 3 shows an example of the averaged results obtained from a CFD simulation when the MUSE method is applied. It can be seen that the averaging process has the effect of decreasing the centerline wind speed deficit and broadening the wake width.

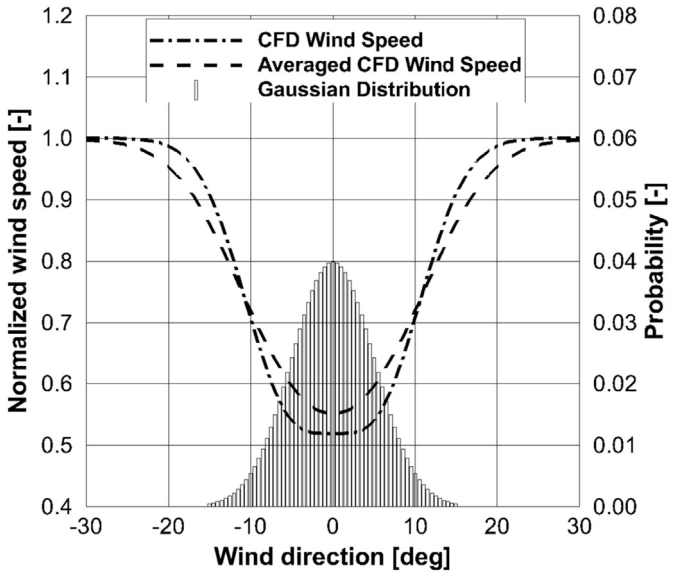

Fig. 3. Example of weighted averaging. A moving weighted averaging process based on a Gaussian distribution is applied to all wind directions. A Gaussian distribution centered at $\overline{\theta} = 0^\circ$ with $\sigma_\theta = 5^\circ$ is plotted for clarification purposes.

Table 3
Root-mean-square errors (RMSE) between the experimental data and the simulations results when considering the wind direction range ±30° for the Sexbierum and Nibe cases, and ±15° for the Horns Rev case. The RMSEs are classified by case (Sexbierum, Nibe, and Horns Rev), by quantity of interest (normalized wind speed (NWS) and normalized power (NP)), by downstream distance, and by turbulence model.

Wind Turbine	Quantity	Distance	$k-\varepsilon$		$k-\omega$	
			Original	MUSE	Original	MUSE
Sexbierum	NWS	2.5*D*	0.1859	0.1890	0.1936	0.1957
		5.5*D*	0.0730	0.0757	0.0804	0.0816
		8*D*	0.0545	0.0556	0.0603	0.0601
Nibe	NWS	2.5*D*	0.1848	0.1910	0.1936	0.1983
		4*D*	0.0683	0.0787	0.0738	0.0814
		7.5*D*	0.0453	0.0536	0.0468	0.0528
Horns Rev	NP	7*D*	0.0247	0.0503	0.0442	0.0798
Wind Turbine	Quantity	Distance	$SSTk-\omega$		RSM	
			Original	MUSE	Original	MUSE
Sexbierum	NWS	2.5*D*	0.0947	0.0933	0.0797	0.0617
		5.5*D*	0.0468	0.0401	0.0462	0.0338
		8*D*	0.0480	0.0435	0.0431	0.0425
Nibe	NWS	2.5*D*	0.0614	0.0694	0.0510	0.0465
		4*D*	0.0619	0.0462	0.0776	0.0582
		7.5*D*	0.0505	0.0401	0.0435	0.0423
Horns Rev	NP	7*D*	0.1349	0.0461	0.0866	0.0392

7. Results and discussion

This section includes the results obtained directly from the CFD RANS simulations and the results obtained after the averaging process with the MUSE method. This comparison aims to highlight the importance of taking into account the wind direction uncertainty when comparing simulation and experimental results. A quantitative comparison, which will be used in the analysis of the results, is made in Table 3 where the root-mean-square errors (RMSE) were calculated between the experimental data and the CFD results. The RMSE is defined according to:

$$RMSE = \sqrt{\frac{\sum_{i=1}^{N}\left(y_{i,exp} - y_{i,CFD}\right)^2}{N}}, \tag{17}$$

where $y_{i,exp}$ and $y_{i,CFD}$ are the experimental and simulated quantities of interest, respectively, and N is the number of experimental observations.

7.1. Simulation results

Figs. 4 and 5 show the normalized wind speed downstream the Sexbierum and Nibe wind turbines, respectively, for different downstream distances and for different turbulence models. The wind direction in the figures refers to the relative direction of the incoming flow where 0° indicates the direction for which the maximum wind speed deficit is expected. In the Sexbierum case, the wind speed was captured well by the *SST* $k-\omega$ and Reynolds stress models for the three locations, whereas was highly overestimated by the $k-\varepsilon$ and $k-\omega$ models, especially at 2.5*D* downstream where the RMSEs were the highest (0.1859 and 0.1936, respectively). The results for the Nibe case showed that the wind speed was captured well by the *SST* $k-\omega$ and Reynolds stress models for the location at 2.5*D* downstream (RMSEs of 0.0614 and 0.0510, respectively), whereas it was underestimated for the other two locations. The $k-\varepsilon$ and $k-\omega$ models, instead, failed to capture the wind speed at 2.5 and 4*D* downstream, whereas more accurate results were obtained in the far wake location.

Fig. 6 show instead the normalized power production of turbine 17 operating in the wake of turbine 07 at the Horns Rev wind farm as a function of wind direction for different turbulence models. In this case, the wind direction is indicated with respect to North, therefore the two turbines are aligned with the incoming flow along a West-East axis at 270°. The calculations of the power production were repeated every 2.5° starting from the direction of 270° where the two turbines were aligned with the incoming wind speed. Because of the scattering in these simulation results, the normalized power distribution was fitted with the following expression:

$$P_n(\theta) = 1 - \left[a_0 + \left(a_1 + a_2\theta + a_3\theta^2\right)\exp\left(-a_4\theta^2\right)\right], \tag{18}$$

where the variables a_0, a_1, a_2, a_3, and a_4 are determined by fitting Eq. (18) to the power values, as function of the normalized wind direction θ (see Fig. 6 for the resulting fitting curves). This fitting function was introduced by Hansen et al. [6] to characterize the power deficit distributions when the results are scattered. The coefficients of the fitting function obtained for each of the normalized power distributions are reported in Table 4. The fitting function is conveniently used in place of the individual power generation data as the input for the MUSE method in the following section. To note in the results for the normalized power production is that the simulations using the $k-\varepsilon$ and $k-\omega$ models were very accurate (RMSEs of 0.0247 and 0.0442, respectively) as opposed to the results obtained with the *SST* $k-\omega$ and Reynolds stress models (RMSEs of 0.1349 and 0.0866, respectively).

The results obtained from the simulations showed the particular characteristics of the turbulence models as well as the inconsistency in wake effect predictions that was found also in literature. The $k-\varepsilon$ and $k-\omega$ models provided very similar results between each other. The only difference between the two models lies in a source term in the ω equation that, in these particular simulations, did not produce a significant contribution. Their inaccuracy, which is usually agreed upon in literature, can be seen particularly in the Sixberium case and in the near wake of the Nibe wind turbine as opposed to the accurate wind speed predictions provided by the *SST* $k-\omega$ and Reynolds stress models. However, the results using

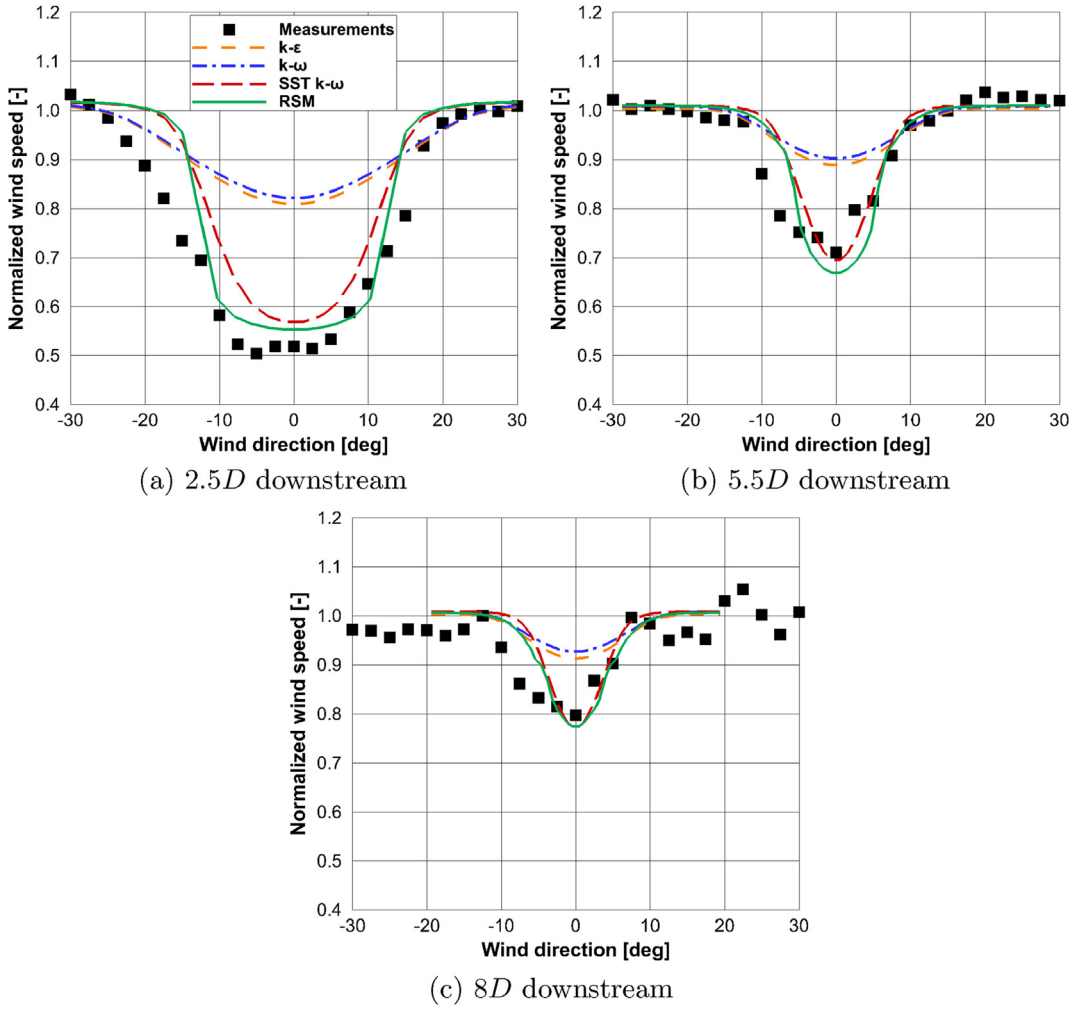

Fig. 4. Normalized wind speed downstream the Sexbierum wind turbine as a function of wind direction for the different turbulence models and for different downstream distance.

the $k-\varepsilon$ and $k-\omega$ models were more accurate that those of the *SST* $k-\omega$ and Reynolds stress models for the far wake of the Nibe wind turbine and for the Horns Rev wind farm.

Better predictions are usually expected by the *SST* $k-\omega$ model and Reynolds stress models. The advantage of the former relies on the bound that is introduced in the eddy viscosity of the model and that overcomes the limitation of its parent models. The RSM has instead the advantage of solving all the Reynolds stresses and therefore it is not affected by the eddy-viscosity approximation. Nevertheless, the results clearly showed that the predictions had high discrepancies for the Horns Rev case and at the locations of 4 and 7.5*D* for the Nibe case.

The discrepancies and the inconsistency of the turbulence models are believed to rely in the wind direction uncertainty, which was not taken into account in the simulations. The result of using the MUSE method is showed in the next section where these limitations are overcome.

7.2. Results with MUSE method

The results from the CFD simulations were post-processed with the MUSE method using a Gaussian distribution for the wind direction uncertainty. An averaging process was used to take into account the wind direction variability characterizing the specific site.

Figs. 8 and 7 show the post-processed wind speed in the wake of the Nibe and Sexbierum wind turbines, respectively. The averaged wind speed from the Sexbierum case did not vary much with respect to the original predictions. This is due to the fact that the wind direction uncertainty was low for this case and the effect on the results was not significant. On the other hand, the averaged results from the Nibe case showed a clear improvement with respect to the original predictions when the *SST* $k-\omega$ and Reynolds stress models were used: at 5.5*D*, the RMSEs decreased from 0.0619 to 0.0776 to 0.0462 and 0.0582, respectively, whereas at 7.5*D*, the RMSEs decreased from 0.0505 to 0.0435 to 0.0401 and 0.0392, respectively. In this case, the wind direction uncertainty was higher and, therefore, a wider range of wind speeds was included in the averaging process, resulting in a more significant effect on the results. As expected, no improvements were registered for the $k-\varepsilon$ and $k-\omega$ models, which were seen to overestimate the wind speed in the original results. The inclusion of the wind speed uncertainty for these two models was even more deleterious for the predictions.

Fig. 9 shows instead the normalized averaged power production of turbine 17 operating in the wake of turbine 07 at the Horns Rev wind farm as a function of wind direction for different turbulence models. The MUSE method was applied to the fitted power distribution curve in order to have more data to process. The results showed a significant difference with respect to the original

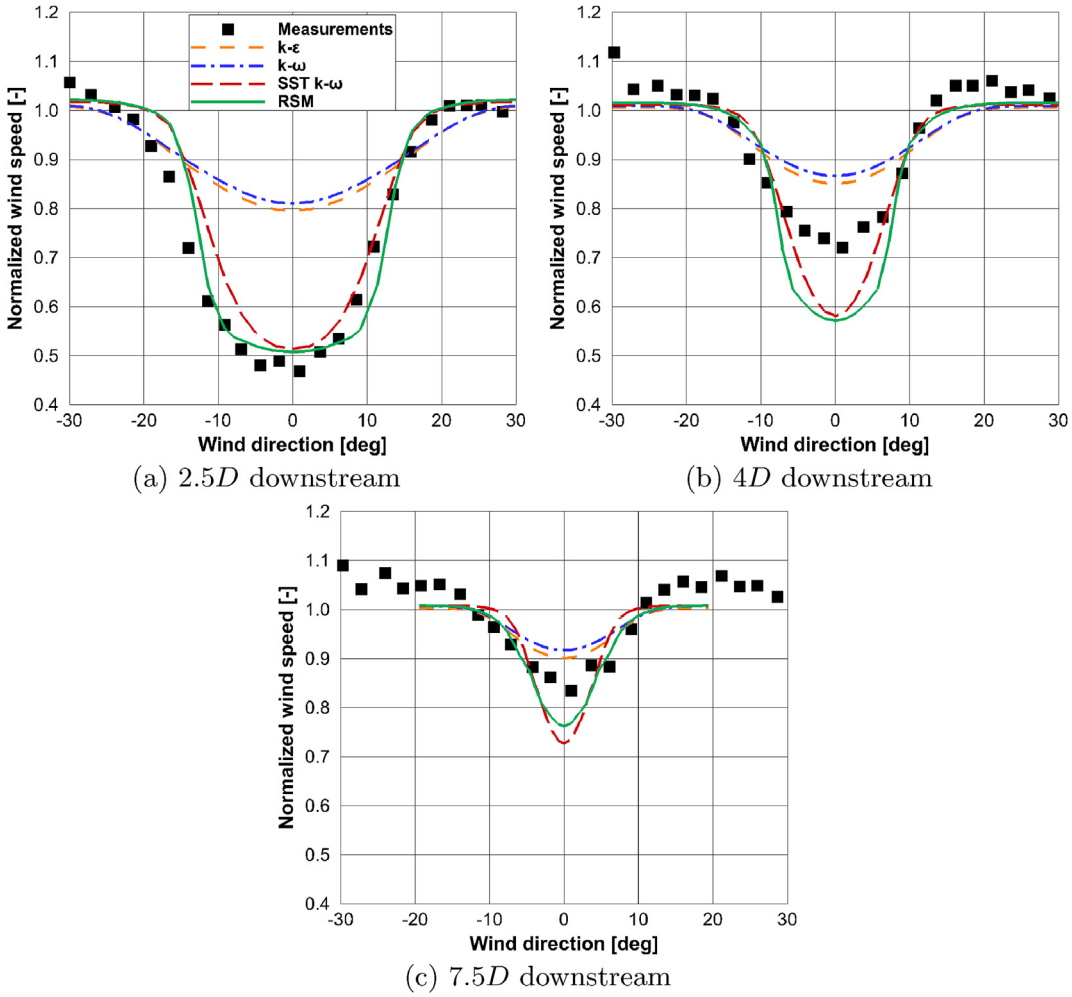

Fig. 5. Normalized wind speed downstream the Nibe wind turbine as a function of wind direction for the different turbulence models and for different downstream distance.

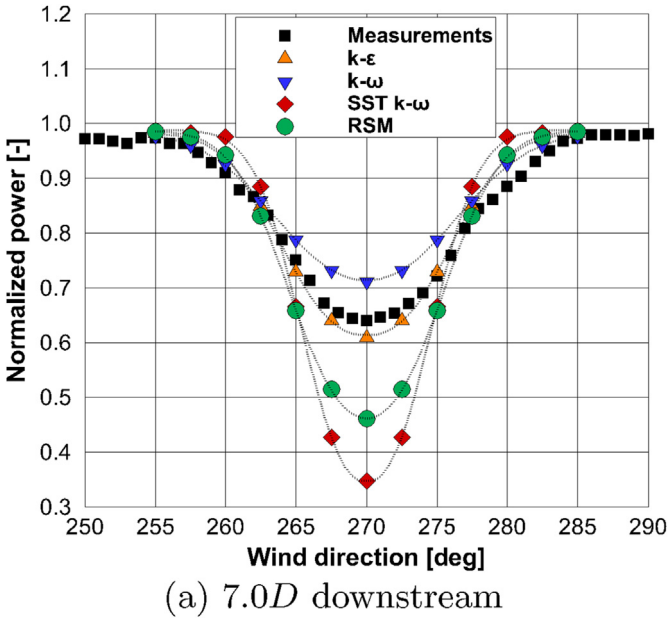

Fig. 6. Normalized power production of turbine 17 operating in the wake of turbine 07 at the Horns Rev wind farm as a function of wind direction for different turbulence models. The continuous lines correspond to Eq. (18) fitted to the normalized power data for each of the turbulence models.

Table 4
Coefficients of the fitting function of Eq. (18) for each of the normalized power distributions plotted in Fig. 6.

	a_0	a_1	a_2	a_3	a_4
$k-\varepsilon$	0.0175	0.3694	0.0004	0.0077	0.0320
$k-\omega$	0.0183	0.2675	0.0004	0.0033	0.0236
$SST\ k-\omega$	0.0126	0.6402	0.0050	0.0178	0.0496
RSM	0.0137	0.5251	0.0000	0.0101	0.0347

simulation results. This is due to the high wind direction uncertainty that was associated with the data set and that was used to post-process the simulation results. It is possible to notice that the predictions of power production given by using the $SST\ k-\omega$ and Reynolds stress models were much more accurate than in the previous case: the RMSEs decreased from 0.1349 to 0.0866 to 0.0461 and 0.0392, respectively. On the other hand, when using the $k-\varepsilon$ and $k-\omega$ models, the post-processed results provided a higher power production and the discrepancy became consistent with the other wind farm simulations (e.g. Refs. [14,18,20]) where the wake wind speed was overestimated.

The inclusion of the wind direction uncertainty with the proposed MUSE method showed that the results directly obtained from the CFD simulation are not always comparable with the experimental observations. This is particularly noticeable in the far wake regions when the wind direction uncertainty was relatively

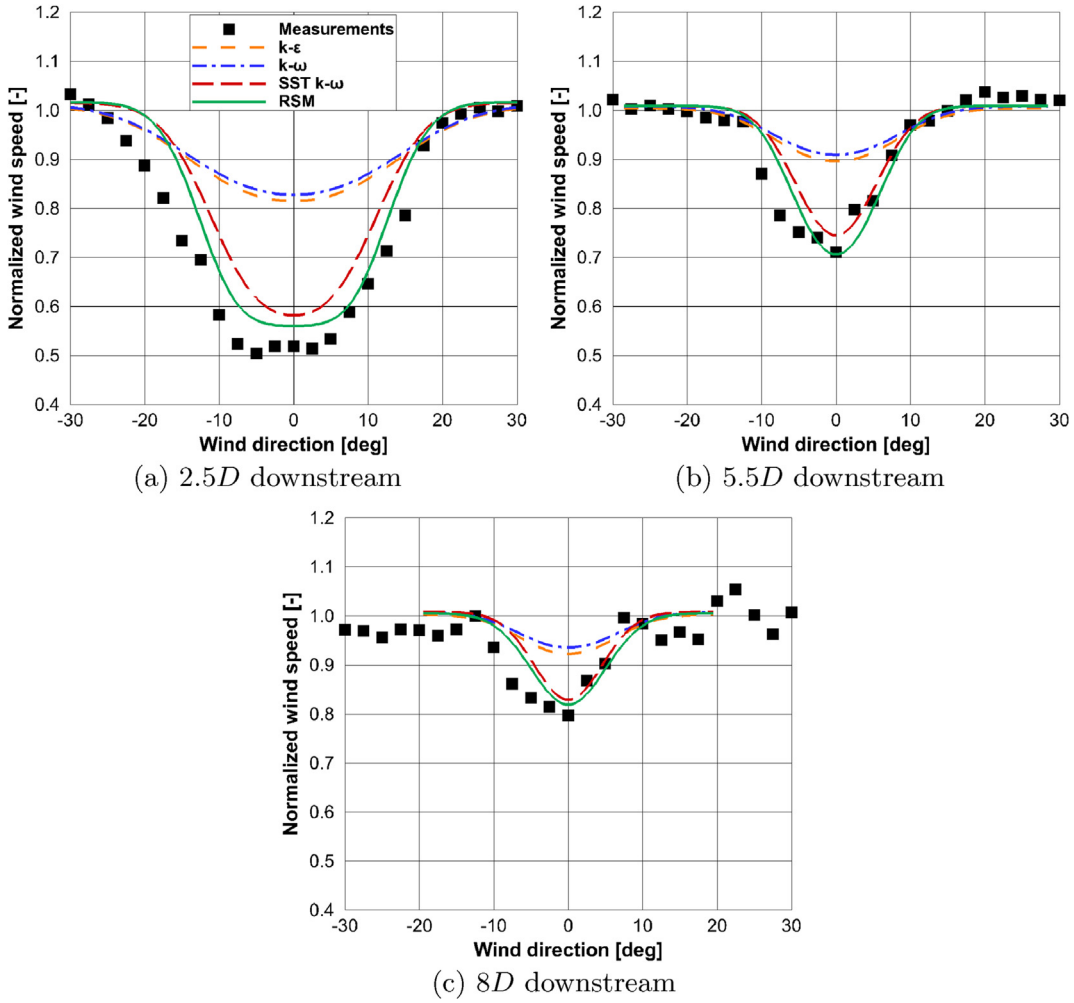

Fig. 7. Normalized averaged wind speed downstream the Sexbierum wind turbine as a function of wind direction for the different turbulence models and for different downstream distance.

high. By using the MUSE method, the RANS simulations using the *SST* $k-\omega$ and Reynolds stress models were shown to be consistently more accurate for wake predictions and are therefore to be preferred over the $k-\varepsilon$ and $k-\omega$ models. This result clarifies and gives an explanation to the sometime inconsistent behavior of the turbulence models highlighted in our results and in the literature. Overall, this method improved the predictions of the CFD RANS model when either of the suggested turbulence models is used. The improvements are more significant where large-scale unsteady phenomena resulted in uncertainty in the wind direction as reported in the experimental data sets.

8. Conclusions

In the present work, we conducted an investigation of the limitations and inconsistency of the RANS wake models in the predictions of wake effects in wind farms. A CFD model was developed which used the actuator disk technique to simulate the wind turbines and the surface boundary layer approximation to simulate the ambient conditions. The developed CFD model was implemented for three different wind farms, namely, Sexbierum, Nibe, and Horns Rev, with publicly available experimental measurements. The main turbulence models present in literature, namely, the $k-\varepsilon$, $k-\omega$, *SST* $k-\omega$ and Reynolds stress models were used to close the RANS equations and their results compared.

The results obtained from the simulations showed the inconsistency in wake effect predictions that was also found in the literature. The simulation using the $k-\varepsilon$ and $k-\omega$ models provided inaccurate predictions for the Sixberium case and in the near wake of the Nibe wind turbine. Despite their known limitations, their results were more accurate for the far wake of the Nibe wind turbine and for the Horns Rev wind farm. On the other hand, the *SST* $k-\omega$ and Reynolds stress models provided opposite results: accurate wind speed predictions for the Sexberium case and in the near wake of the Nibe wind turbine and high discrepancies for the Horns Rev wind farm.

The discrepancies and the inconsistency of the turbulence models were hypothesized to arise from wind direction uncertainty caused by large-scale unsteady phenomena, which though present in the experimental measurements were not accounted for in the simulations. We therefore proposed an approach to overcome these limitations by Modeling Uncertainty using Simulation Ensembles (MUSE), i.e., a set of CFD results for different wind directions to generate a single CFD prediction. The predictions of CFD model were post-processed with this innovative method for CFD simulations that accounts for the wind direction uncertainty associated with the specific wind farm data set. In this way, the local characteristics of the wind direction variability that affected the experimental measurements can be properly accounted for. The proposed

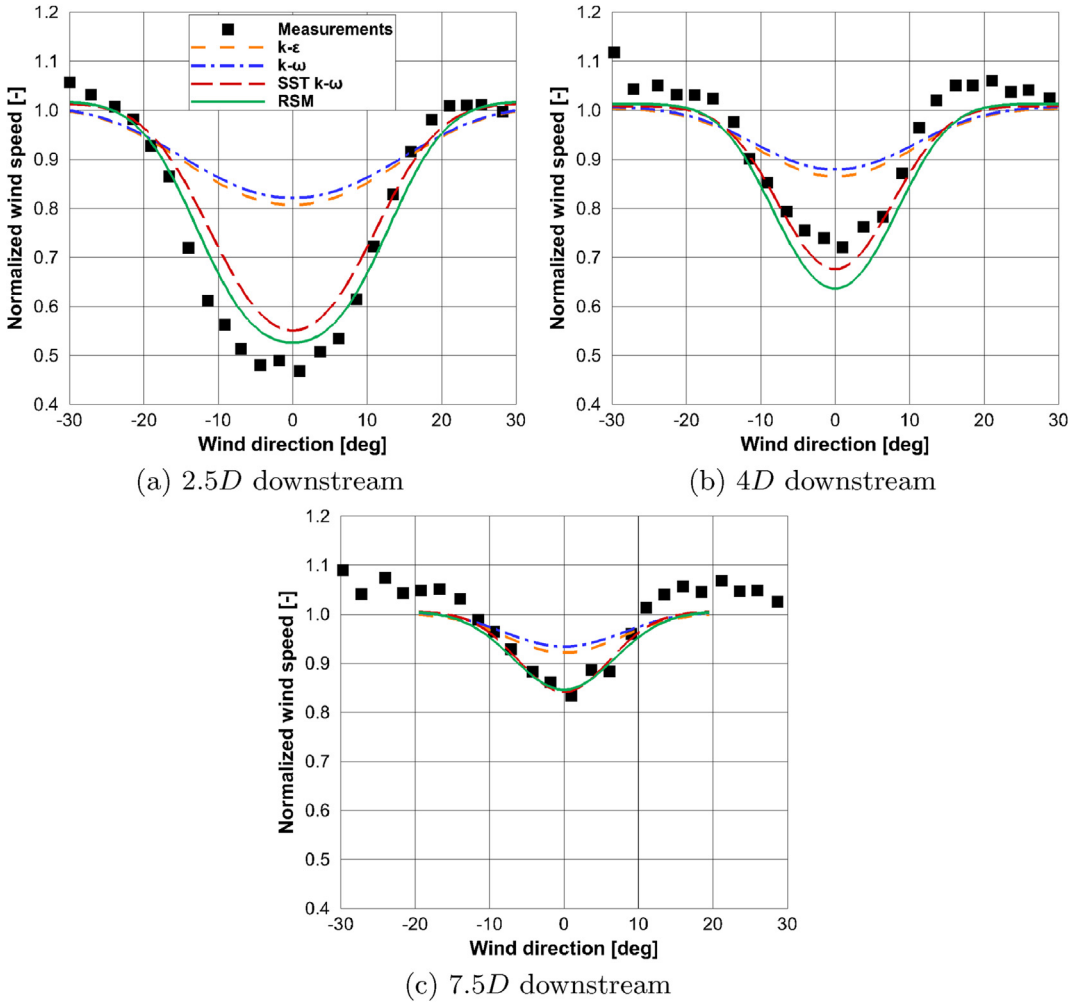

Fig. 8. Normalized averaged wind speed downstream the Nibe wind turbine as a function of wind direction for the different turbulence models and for different downstream distance.

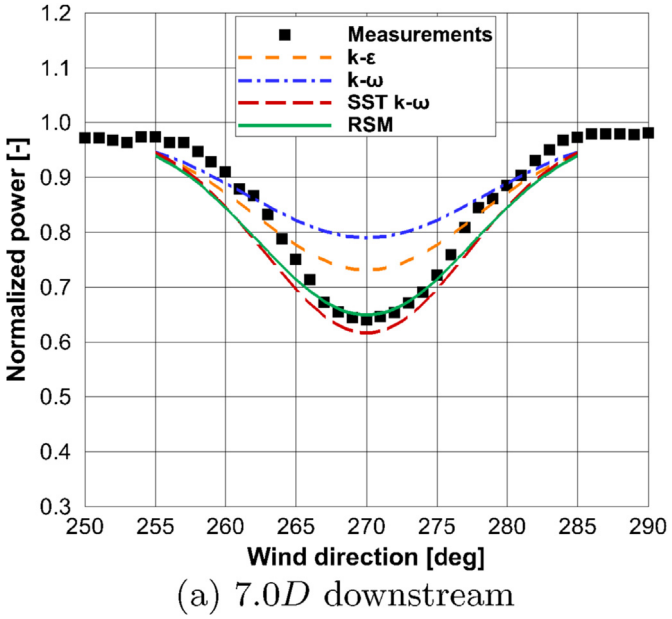

Fig. 9. Normalized averaged power production of turbine 17 operating in the wake of turbine 07 at the Horns Rev wind farm as a function of wind direction for different turbulence models.

MUSE method can be considered a computationally faster alternative to URANS or LES models, when the goal is to account for the effect of large-scale, transient flow phenomena causing wind direction variability.

The results in terms of wind speed and power output showed that this technique corrects the predictions of the CFD model which would be otherwise inaccurate. Specifically, RANS simulations using the *SST* $k-\omega$ and Reynolds stress models were shown to be consistently more accurate for wake predictions and are therefore to be preferred over the $k-\varepsilon$ and $k-\omega$ models. The results showed also that the discrepancy found between CFD models using the *SST* $k-\omega$ or Reynolds stress models and field measurements are not related to the inaccuracy of the CFD models but to the uncertainty embedded in the time-averaged wind direction measurements.

References

[1] Global Wind Energy Council, Global Wind Report, 2016.
[2] R.J. Barthelmie, S.T. Frandsen, M.N. Nielsen, S.C. Pryor, P.-E. Réthoré, H.E. Jørgensen, Modelling and measurements of power losses and turbulence intensity in wind turbine wakes at Middelgrunden offshore wind farm, Wind Energy 10 (6) (2007) 517–528, https://doi.org/10.1002/we.238.
[3] R.J. Barthelmie, S.C. Pryor, S.T. Frandsen, K.S. Hansen, J.G. Schepers, K. Rados, W. Schlez, A. Neubert, L.E. Jensen, S. Neckelmann, Quantifying the impact of wind turbine wakes on power output at offshore wind farms, J. Atmos. Ocean.

Technol. 27 (8) (2010) 1302–1317, https://doi.org/10.1175/2010JTECHA1398.1.
[4] R.J.A.M. Stevens, C. Meneveau, Flow structure and turbulence in wind farms, Annu. Rev. Fluid Mech. 49 (1) (2017) 311–339, https://doi.org/10.1146/annurev-fluid-010816-060206.
[5] S.P. Sanderse, B. andvan der Pijl, B. Koren, Review of computational fluid dynamics for wind turbine wake aerodynamics, Wind Energy 2011 (14) (2011) 799–819, https://doi.org/10.1002/we.458.
[6] K.S. Hansen, R.J. Barthelmie, L.E. Jensen, J. Mann, A. Sommer, The impact of turbulence intensity and atmospheric stability on power deficits due to wind turbine wakes at Horns Rev wind farm, Wind Energy 15 (2012) 183–196, https://doi.org/10.1002/we.512.
[7] A. Westerhellweg, B. Cañadillas, F. Kinder, T. Neumann, Wake measurements at alpha ventus - dependency on stability and turbulence intensity, J. Phys. Conf. 555. doi:10.1088/1742-6596/555/1/012106.
[8] L.J. Vermeer, J.N. Sørensen, A. Crespo, Wind turbine wake aerodynamics, Prog. Aero. Sci. 39 (6–7) (2003) 467–510, https://doi.org/10.1016/S0376-0421(03)00078-2.
[9] A. Crespo, J. Hernández, S. T. a. Frandsen, Survey of modelling methods for wind turbine wakes and wind farms, Wind Energy 2 (1) (1999) 1–24, https://doi.org/10.1002/(SICI)1099-1824(199901/03)2:1<1::AID-WE16>3.0.CO;2-7.
[10] J.Y. Kuo, D.A. Romero, J.C. Beck, C.H. Amon, Wind farm layout optimization on complex terrains Integrating a CFD wake model with mixed-integer programming, Appl. Energy 178 (2016) 404–414, https://doi.org/10.1016/j.apenergy.2016.06.085.
[11] E.G.A. Antonini, D.A. Romero, C.H. Amon, Continuous adjoint formulation for wind farm layout optimization: a 2D implementation, Appl. Energy 228 (2018) 2333–2345, https://doi.org/10.1016/j.apenergy.2018.07.076.
[12] A. Crespo, J. Hernández, Numerical modelling of the flow field in a wind turbine wake, in: Proceedings of the 3rd Joint ASCE/ASME Mechanics Conference, Forum on Turbulent Flows., La Jolla, CA, USA, 1989.
[13] P.-E. Réthoré, Wind Turbine Wake in Atmospheric Turbulence, Ph.D. thesis, Aalborg University, Aalborg, Denmark, 2009.
[14] D. Cabezón, E. Migoya, A. Crespo, Comparison of turbulence models for the computational fluid dynamics simulation of wind turbine wakes in the atmospheric boundary layer, Wind Energy 14 (7) (2011) 909–921, https://doi.org/10.1002/we.516.
[15] E.S. Politis, J.M. Prospathopoulos, D. Cabezón, K.S. Hansen, P.K. Chaviaropoulos, R.J. Barthelmie, Modeling wake effects in large wind farms in complex terrain: the problem, the methods and the issues, Wind Energy 15 (1) (2012) 161–182, https://doi.org/10.1002/we.481.
[16] J.M. Prospathopoulos, E.S. Politis, P.K. Chaviaropoulos, Modelling wind turbine wakes in complex terrain, in: European Wind Energy Conference and Exhibition, Brussels, Belgium, 2008. https://www.researchgate.net/profile/John_Prospathopoulos/publication/228403867_Modelling_wind_turbines_in_complex_terrain/links/0046351650fff25b59000000.pdf.
[17] J.M. Prospathopoulos, E.S. Politis, K.G. Rados, P.K. Chaviaropoulos, Evaluation of the effects of turbulence model enhancements on wind turbine wake predictions, Wind Energy 14 (2) (2011) 285–300, https://doi.org/10.1002/we.419.
[18] M. Shives, C. Crawford, Adapted two-equation turbulence closures for actuator disk RANS simulations of wind and tidal turbine wakes, Renew. Energy 92 (2016) 273–292, https://doi.org/10.1016/j.renene.2016.02.026.
[19] E.G.A. Antonini, D.A. Romero, C.H. Amon, Analysis and modifications of turbulence models for wind turbine wake simulations in atmospheric boundary layers, in: Proceedings of the ASME 2016 International Mechanical Engineering Congress and Exposition, Phoenix, Arizona, USA, 2016, https://doi.org/10.1115/IMECE2016-67353.
[20] E.G.A. Antonini, D.A. Romero, C.H. Amon, Analysis and modifications of turbulence models for wind turbine wake simulations in atmospheric boundary layers, J. Sol. Energy Eng. 140 (2018) 031007, https://doi.org/10.1115/1.4039377.
[21] A. El Kasmi, C. Masson, An extended $k-\varepsilon$ model for turbulent flow through horizontal-axis wind turbines, J. Wind Eng. Ind. Aerod. 96 (2008) 103–122, https://doi.org/10.1016/j.jweia.2007.03.007.
[22] M.P. van der Laan, N.N. Sørensen, P.-E. Réthoré, J. Mann, M.C. Kelly, N. Troldborg, J.G. Schepers, E. Machefaux, An improved $k-\varepsilon$ model applied to a wind turbine wake in atmospheric turbulence, Wind Energy 18 (5) (2015) 889–907, https://doi.org/10.1002/we.1736.
[23] R.J. Barthelmie, K.S. Hansen, S.T. Frandsen, O. Rathmann, J.G. Schepers, W. Schlez, J. Phillips, K.G. Rados, A. Zervos, E.S. Politis, P.K. Chaviaropoulos, Modelling and measuring flow and wind turbine wakes in large wind farms offshore, Wind Energy 10 (6) (2007) 517–528, https://doi.org/10.1002/we.238.
[24] M. Gaumond, P.-E. Réthoré, S. Ott, A. Peña, A. Bechmann, K.S. Hansen, Evaluation of the wind direction uncertainty and its impact on wake modeling at the Horns Rev offshore wind farm, Wind Energy 17 (8) (2014) 1169–1178, https://doi.org/10.1002/we.1625.
[25] J. Kiviluoma, H. Holttinen, D. Weir, R. Scharff, L. Söder, N. Menemenlis, N.A. Cutululis, I. Danti Lopez, E. Lannoye, A. Estanqueiro, E. Gomez-Lazaro, Q. Zhang, J. Bai, Y.-H. Wan, M. Milligan, Variability in large-scale wind power generation, Wind Energy 19 (9) (2016) 1649–1665, https://doi.org/10.1002/we.1942.
[26] F. Porté-Agel, Y.T. Wu, C.H. Chen, A numerical study of the effects of wind direction on turbine wakes and power losses in a large wind farm, Energies 6 (10) (2013) 5297–5313, https://doi.org/10.3390/en6105297.
[27] J.W. Cleijne, Results of Sexbierum Wind Farm; Single Wake Measurements, Tech. Rep. 93-082, TNO Institute of Environmental and Energy Technology, Apedoorn, The Netherlands, 1993.
[28] G.J. Taylor, Wake Measurements on the Nibe Wind Turbines in Denmark, Tech. Rep. ETSU WN 5020, National Power - Technology and Environment Center, London, England, 1990.
[29] A. Peña, P.-E. Réthoré, C. B. a. Hasager, Results of Wake Simulations at the Horns Rev I and Lillgrund Wind Farms Using the Modified Park Model, Tech. Rep. 26, DTU Wind Energy, Roskilde, Denmark, 2013.
[30] The OpenFOAM Foundation Ltd, OpenFOAM 2.4.0, http://www.openfoam.org/, accessed: June 2016.
[31] W.P. Jones, B.E. Launder, The prediction of laminarization with a two-equation model of turbulence, Int. J. Heat Mass Tran. 15 (2) (1972) 301–314, https://doi.org/10.1016/0017-9310(72)90076-2.
[32] B.E. Launder, B.I. Sharma, Application of the energy dissipation model of turbulence to the calculation of flow near a spinning disc, Lett. Heat Mass Tran. 1 (2) (1974) 131–137, https://doi.org/10.1016/0094-4548(74)90150-7.
[33] S.B. Pope, Turbulent Flows, Cambridge University Press, 2000.
[34] D.C. Wilcox, Turbulence Modeling for CFD, second ed., DCW Industries, 1994.
[35] D.C. Wilcox, Reassessment of the scale-determining equation for advanced turbulence models, AIAA J. 26 (11) (1988) 1299–1310, https://doi.org/10.2514/3.10041.
[36] F.R. Menter, Two-equation eddy-viscosity turbulence models for engineering applications, AIAA J. 32 (8) (1994) 1598–1605, https://doi.org/10.2514/3.12149.
[37] P.A. Durbin, B.A. Pettersson Reif, Statistical Theory and Modeling for Turbulent Flows, second ed., John Wiley & Sons, 2011.
[38] B.E. Launder, G.J. Reece, W. Rodi, Progress in the development of Reynolds-stress turbulence closure, J. Fluid Mech. 68 (3) (1975) 537–566, https://doi.org/10.1017/S0022112075001814.
[39] C.B. Speziale, S. Sarkar, T.B. Gatski, Modelling the pressure strain correlation of turbulence: an invariant dynamical systems approach, J. Fluid Mech. 227 (1991) 245–272, https://doi.org/10.1017/S0022112091000101.
[40] M.M. Gibson, B.E. Launder, Ground effects on pressure fluctuations in the atmospheric boundary layer, J. Fluid Mech. 86 (3) (1978) 491–511, https://doi.org/10.1017/S0022112078001251.
[41] J.N. Sørensen, A. Myken, Unsteady actuator disc model for horizontal axis wind turbines, J. Wind Eng. Ind. Aerod. 39 (1–3) (1992) 139–149, https://doi.org/10.1016/0167-6105(92)90540-Q.
[42] I. Ammara, C. Leclerc, C. Masson, A viscous three-dimensional differential/actuator-disk method for the aerodynamic analysis of wind farms, J. Sol. Energy Eng. 124 (4) (2002) 345–356, https://doi.org/10.1115/1.1510870.
[43] H.A. Panofsky, J.A. Dutton, Atmospheric Turbulence: Models and Methods for Engineering Applications, John Wiley & Sons, 1984.
[44] S.-E. Gryning, E. Batchvarova, B. Brümmer, H. Jørgensen, S. Larsen, On the extension of the wind profile over homogeneous terrain beyond the surface boundary layer, Boundary-Layer Meteorol. 124 (2) (2007) 251–268, https://doi.org/10.1007/s10546-007-9166-9.
[45] P.J. Richards, R.P. Hoxey, Appropriate boundary conditions for computational wind engineering models using the k-epsilon turbulence model, J. Wind Eng. Ind. Aerod. 46–47 (1993) 145–153, https://doi.org/10.1016/0167-6105(93)90124-7.
[46] B. Blocken, T. Stathopoulos, J. Carmeliet, CFD simulation of the atmospheric boundary layer: wall function problems, Atmos. Environ. 41 (2) (2007) 238–252, https://doi.org/10.1016/j.atmosenv.2006.08.019.
[47] G. España, S. Aubrun, S. Loyer, P. Devinant, Wind tunnel study of the wake meandering downstream of a modelled wind turbine as an effect of large scale turbulent eddies, J. Wind Eng. Ind. Aerod. 101 (2012) 24–33, https://doi.org/10.1016/j.jweia.2011.10.011.
[48] M. Gaumond, P.-E. Réthoré, A. Bechmann, S. Ott, G.C. Larsen, A. Peña, K.S. Hansen, Benchmarking of wind turbine wake models in large offshore wind farms, in: The Science of Making Torque from Wind, Oldenburg, Germany, 2012. http://www.eera-dtoc.eu/wp-content/uploads/files/Gaumond-et-al-Benchmarking-of-wind-turbine-wake-models-in-large-offshore-wind-farms5.pdf.
[49] A. Peña, P.-E. Réthoré, M.P. van del Lann, On the application of the Jensen wake model using a turbulence-dependent wake decay coefficient: the Sexbierum case, Wind Energy 19 (4) (2016) 763–776, https://doi.org/10.1002/we.1863.